Trimer superfluidity of antiparallel dipolar excitons in a bilayer heterostructure

Pradyumna P. Belgaonkar[1], Michal Zimmerman[1], Snir Gazit[1,2], and Dror Orgad[1]
[1] *Racah Institute of Physics, The Hebrew University of Jerusalem, Jerusalem 9190401, Israel*
[2] *The Fritz Haber Research Center for Molecular Dynamics, The Hebrew University of Jerusalem, Jerusalem 9190401, Israel*
(Dated: July 22, 2026)

We study the phase diagram of a bilayer of antiparallel dipolar excitons with a 1:2 density ratio between the layers, as a function of temperature and density. Using quantum Monte Carlo simulations, we show that such a system supports the formation of trimers, namely, three-exciton bound states consisting of a single dipole in one layer and two dipoles in the second layer. At sufficiently low temperatures and densities, these trimers condense into a trimer superfluid phase. Increasing the excitonic density induces a quantum phase transition into a phase in which condensates of independent dipoles exist in both layers, in parallel to the trimers. We also study the thermal transitions out of these phases, and find that while the normal state is reached directly from the trimer superfluid, the thermal disordering of the two-superfluid phase involves an intermediate state which is either a trimer superfluid or a single excitonic condensate in the denser layer. A potential experimental realization using transition metal dichalcogenide heterostructures is discussed.

arXiv:2507.15938v2 [cond-mat.mes-hall] 21 Jul 2026

I. INTRODUCTION

Dipolar interactions in quantum many-body systems give rise to a rich variety of exotic collective behavior. Their anisotropic character, where forces can be either repulsive or attractive depending on the relative dipolar orientation and inter-particle separation, coupled with their long-range nature, can stabilize unconventional excitations and promote strong correlations.

Dipolar systems have been extensively investigated experimentally in ultracold atomic gases with either magnetic or electric dipole moments [1, 2]. In the low temperature regime, experiments have demonstrated Bose-condensed states [3–5] and, more recently, supersolid phases [6–8]. In the solid-state realm, dipolar excitons constitute a particularly promising platform for enhancing correlations due to their relatively high density and pronounced electrostatic interactions. Achieving a permanent dipole moment requires spatial separation of electrons and holes. In semiconductor heterostructures, this is often achieved in a double quantum well subjected to an external electric field, which orients the dipoles [9, 10]. However, an emerging alternative utilizes transition metal dichalcogenide (TMD) heterostructures, where the layering itself determines the dipole orientation, even in the absence of an aligning field [11].

Exposing the anisotropic nature of dipolar interactions requires structures that go beyond a single layer of dipoles. A simple extension involves stacking a pair of double quantum wells, as realized in a semiconducting quadrilayer systems [12, 13]. Indeed, the attractive interlayer interaction between parallel dipoles was observed experimentally. Interestingly, a sufficiently strong attraction is predicted to support the formation of a dimer superfluid comprising bound interlayer molecules [14].

The versatility of TMD-based systems opens up the possibility to engineer the dipole orientation of each layer independently. In particular, arranging antiparallel dipoles results in inverted interlayer interactions relative to the previously studied parallel case. The collective behavior of quantum antiparallel dipoles holds the promise of realizing new phases of composite particles.

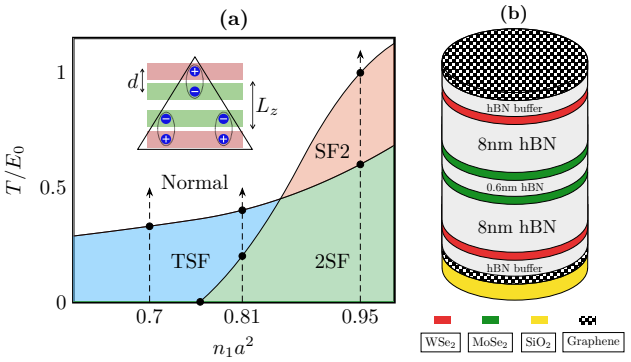


FIG. 1: (a) The phase diagram of a bilayer of antiparallel dipolar excitons with 1:2 density ratio, as depicted in the inset. The phases include a trimer superfluid (TSF), independent superfluids in the two layers (2SF) and a superfluid in layer 2 (SF2). The critical temperatures along the dashed lines were calculated for the TMD-based heterostructure whose parameters are specified in (b). The graphene layers enable electrical gating.

In this work, we investigate a quadrilayer structure that realizes a bilayer of oppositely oriented dipoles. Using numerically exact large-scale quantum Monte Carlo simulations, we determine the low-temperature phase diagram of such a system, specifically at a 1:2 filling ratio between the layers. In the vicinity of this point, excitons tend to form trimers, namely three-exciton interlayer bound states that exploit the attractive component of the dipolar interaction. At low temperatures and in the dilute limit, these trimers condense, forming a phase that partially breaks the global $U(1) \times U(1)$ symmetry down to $U(1)$. Upon increasing the density, we identify a zero-temperature BEC quantum phase transition, where the residual $U(1)$ symmetry breaks. The finite-temperature phase diagram exhibits a rich structure

featuring Berezinskii–Kosterlitz–Thouless (BKT) transitions between composite and elementary superfluids. In addition, we also comment on the nature of the phase diagram away from the 1:2 point, discuss the experimental aspects involved in realizing the model in TMD heterostructurs, and outline observable signatures of trimers and their condensation.

II. MODEL

We model the many-exciton system within the quadrilayer structure shown in Fig. 1 as a collection of point-like dipolar bosons arranged in two layers separated by distance L_z. This approximation is valid in the dilute limit, where the extent of the exciton wavefunction is small compared to the inter-exciton separation. The dipole moments in the top (bottom) layer are pointed in the positive (negative) $\hat{z}$ direction, due to the mirror symmetry of the quadrilayer. Neglecting tunneling between layers, the dynamics follows the Hamiltonian

$$\mathcal{H} = -\frac{\hbar^2}{2m_X}\sum_{i,\alpha}\nabla^2_{i,\alpha} + \frac{D^2}{2}\sum_{i_\alpha \neq j_\beta} V\left(\mathbf{r}_{i_\alpha}, \mathbf{r}_{j_\beta}\right), \qquad (1)$$

where m_X is the effective exciton mass and the dipole strength $D^2 = e^2d^2/\varepsilon$ is given in terms of the exciton dipole moment ed and the permittivity ε. We label excitons by i_α, with $\alpha = 1, 2$ denoting their layer index, and $\mathbf{r}_{i_\alpha}$ their *in-plane* position. Assuming that the excitonic densities $n_\alpha = N_\alpha/A$ obey $n_\alpha d^2 \ll 1$ their dipolar interaction takes the form

$$V\left(\mathbf{r}_{i_\alpha}, \mathbf{r}_{j_\beta}\right) = \begin{cases} 1/\left|\mathbf{r}_{i_\alpha} - \mathbf{r}_{i_\beta}\right|^3, & \alpha = \beta \\ -\frac{\left|\mathbf{r}_{i_\alpha} - \mathbf{r}_{i_\beta}\right|^2 - 2L_z^2}{\left(\left|\mathbf{r}_{i_\alpha} - \mathbf{r}_{i_\beta}\right|^2 + L_z^2\right)^{\frac{5}{2}}}, & \alpha \neq \beta. \end{cases} \qquad (2)$$

Henceforth, we measure lengths and energies in units of $a = m_X D^2/\hbar^2$ and $E_0 = D^2/a^3$, respectively. To maintain contact with the physical systems, we note that $a = 183$ nm and $E_0 = 4.54$ μeV for a $d = 8$ nm $MoSe_2$-WSe_2 structure [15–20], see Fig. 1b.

III. THREE-BODY BOUND STATE

We begin our analysis by establishing the presence of a trimer bound state. Crucial for its formation is the spatial structure of the interlayer interaction. Initially repulsive at short distances, it becomes attractive for separations larger than $\sqrt{2}L_z$. This allows the two excitons in the bottom layer to bind to the exciton in the top layer while avoiding their strong short-distance intralayer repulsion. The total interaction potential seen by the bottom layer excitons attains a minimum when their mutual separation is $4.28L_z$. This distance may be taken as a rough estimate for the diameter of the trimer.

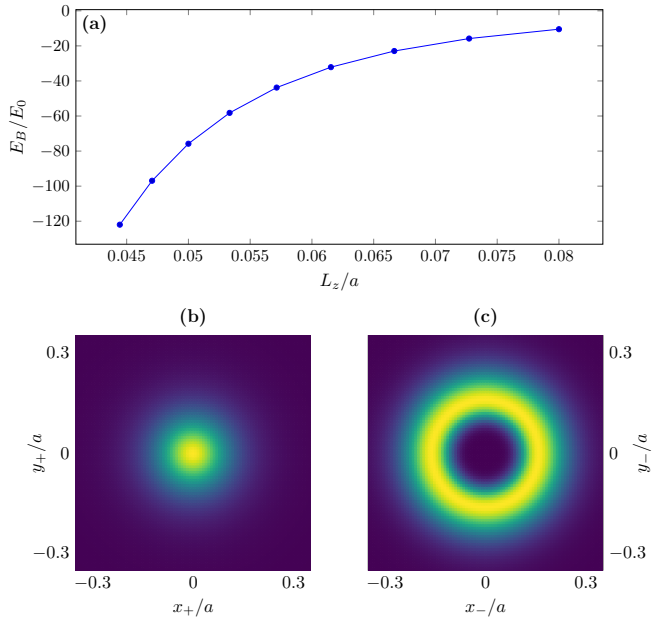


FIG. 2: The trimer bound state. (a) The binding energy as a function of L_z/a. (b) and (c) The probability distribution functions $|\psi_+(\mathbf{r}_+)^2|$ and $|\psi_-(\mathbf{r}_-)|^2$ for the case $L_z/a = 0.047$.

It is useful to contrast the above discussion with the case of parallel dipoles [14], where the interlayer attraction peaks at zero separation, precisely where the intralayer repulsion diverges.

To substantiate the above scenario, we diagonalized numerically the Hamiltonian, Eq. (1), and obtained the three-exciton ground state. The results, shown in Fig. 2, clearly demonstrate a trimer bound state, whose binding energy decreases monotonically with L_z/a. We present its structure using the coordinates $\mathbf{r}_+ = (\mathbf{r}_2 + \mathbf{r}_3)/2 - \mathbf{r}_1$ and $\mathbf{r}_- = (\mathbf{r}_2 - \mathbf{r}_3)/2$, defined in terms of the positions $\mathbf{r}_1$ and $\mathbf{r}_{2,3}$ of the excitons in the upper and lower layers, respectively. The probability distribution function $|\psi_+(\mathbf{r}_+)|^2 = \int d^2r_- |\psi(\mathbf{r}_+, \mathbf{r}_-)|^2$ is centered at $\mathbf{r}_+ = 0$, indicating a symmetric configuration of the lower particles around $\mathbf{r}_1$, see Fig. 2b. Concomitantly, $|\psi_-(\mathbf{r}_-)|^2 = \int d^2r_+ |\psi(\mathbf{r}_+, \mathbf{r}_-)|^2$ reveals that $\mathbf{r}_{2,3}$ largely occupy antipodal points on a ring, whose diameter for the case $L_z/a = 0.047$ shown in Fig. 2c is 60% larger than the classical trimer diameter. This is due to the slow decay of the interaction potential at large separations.

The interlayer interaction enables the formation of other bound states comprising one upper-layer exciton and $n-1$ lower-layer excitons. Classically, the minimum energy for such an n-mer is achieved in a static configuration where the upper exciton is positioned directly above the center of a regular $(n-1)$-sided polygon, with the lower-layer excitons at its vertices. The binding energy is expected to diminish with n because the number of repulsive lower-layer pairs grows quadratically as $\binom{n-1}{2}$, whereas the attractive interlayer component scales only as $n-1$. Indeed, we find that the classical binding energy maximizes for the trimer and subsequently decreases

for $n \geq 4$. The classical binding-energy of the dimer is approximately 40% smaller than that of the trimer, a consequence of the trimer's additional attractive interlayer interaction overcoming its intralayer repulsion for sufficiently separated lower-layer excitons. Quantum mechanically, the uncertainty principle smears the classical configuration, introducing a kinetic energy contribution that grows with n and reduces the binding energy. Consequently, the quantum binding energy of the dimer is only 20% smaller than that of the trimer (see Appendix A), but the trimer still emerges as the most favorable complex of anti-parallel excitons within the bilayer structure.

IV. TRIMER CONDENSATE AND ITS DENSITY DRIVEN QUANTUM PHASE TRANSITION

In light of the above discussion, a simple energetic argument suggests the existence of a trimer liquid at the commensurate ratio $n_2/n_1 = 2$ between the excitonic densities, at least in the dilute limit $n_\alpha a^2 \ll 1$ where the interaction between trimers is weak and is likely unable to destabilize the bound states. Consequently, we focus on the case $n_2/n_1 = 2$, and comment on the physics away from this point in the Discussion section.

At sufficiently low temperatures below a BKT transition, the trimers are expected to condense into a trimer superfluid state (TSF). At zero temperature the TSF is characterized by partial breaking of the global $U(1) \times U(1)$ symmetry, associated with the independent conservation of particle number in each layer. Specifically, the TSF order parameter $\mathcal{O}_{\rm TSF} = \langle b_1 b_2 b_2 \rangle = \sqrt{\rho_T} e^{i\theta_+}$, expressed in terms of the exciton annihilation operators $b_\alpha \sim e^{i\theta_\alpha}$, acquires a nonzero vacuum expectation value, which locks the phase variable $\theta_+ = \theta_1 + 2\theta_2$. By contrast, the complementary angle variable, $\theta_- = 2\theta_1 - \theta_2$, fluctuates and together with $\theta_{1,2}$, remains disordered.

In the dense limit $n_\alpha a^2 \gg 1$ the repulsive intralayer interaction dominates over the interlayer attraction and is expected to cause dissociation of the trimers. In this limit the layers decouple and can condense into two independent superfluids, thus breaking the remaining $U(1)$ symmetry and establishing order in both θ_+ and θ_- (or equivalently in $\theta_{1,2}$.) We note, however, that the transition out of the TSF at $n_1 = n_c$ does not necessarily imply significant dissociation of the bound states. Instead, independent superflow of excitons may emerge in parallel to the superflow of trimers, without compromising the integrity of the latter. Such a phase exhibits the same symmetry breaking pattern as the state of two completely independent superfluids, and we denote them both by 2SF. They can be distinguished by the presence of non vanishing interlayer drag.

To elucidate the properties of the many-exciton system we use path integral Monte Carlo (PIMC) simulations [21], and specifically the worm algorithm [22]. We establish the ground state properties by tracking the convergence of the finite-temperature results when we lower the temperature T and increase the total number of particles to $N_{\rm tot} = 36$. To detect the onset of order we calculate the superfluid stiffness tensor $\rho_{\alpha\beta} = \partial^2 F / \partial\Phi_\alpha \partial\Phi_\beta$, measuring the response of the free energy F of a system on a torus to the insertion of Aharonov-Bohm fluxes, Φ_α, minimally coupled to layer α. An eigenmode of $\rho_{\alpha\beta}$ with a nonzero eigenvalue in the $T = 0$, $N \to \infty$ limit, corresponds to the phase of an order parameter that breaks a $U(1)$ symmetry, while a zero-mode is associated with a conserved $U(1)$ charge. In practice, we calculate the stiffness via the winding numbers $\mathbf{W}_\alpha = \{W_\alpha^x, W_\alpha^y\}$ of the world lines of layer-α particles around the x, y directions using $\rho_{\alpha\beta} = T\langle \mathbf{W}_\alpha \cdot \mathbf{W}_\beta \rangle / 2$ [23]. The phases $\theta_\pm$ couple to $\Phi_+ = \Phi_1 + 2\Phi_2$ and $\Phi_- = 2\Phi_1 - \Phi_2$. Correspondingly, the stiffness of θ_+ is given by $\rho_+ = T\langle (\mathbf{W}_1 + 2\mathbf{W}_2)^2 \rangle / 50$. Whenever θ_+ orders, the vortices responsible for disordering θ_- involve 10π phase windings (see next section and Appendix H). The stiffness that is relevant to their proliferation is given by the response to $\Phi_-/5$ and takes the form $\rho_- = T\langle (2\mathbf{W}_1 - \mathbf{W}_2)^2 \rangle / 2$.

Fig. 3 provides evidence for a TSF phase. In particular, it depicts the temperature dependence of $\rho_\pm$ for a system with $L_z/a = 0.047$ and $n_1 = 0.7/a^2$. Clearly, the low-temperature ρ_+ remains above the BKT line $\rho = 2T/\pi$ as the number of excitons increases, signaling the establishment of θ_+ quasi-long-range order (QLRO). Conversely, the finite size scaling of ρ_- indicates its disappearance in the thermodynamic limit, see Appendix B. Further supporting evidence comes from the distribution of $W_+ = W_1 + 2W_2$ that peaks at multiples of 5, indicating the correlated winding of excitons as composites comprising a single exciton in the top layer ($W_1 = 1$) and a pair of excitons in the bottom layer ($W_2 = 2$).

Finally, we evaluate the density-density correlation functions $g_{\alpha\beta}(\mathbf{r}) = A/(N_\alpha N_\beta) \sum_{i_\alpha \neq j_\beta} \langle \delta(\mathbf{r} - \mathbf{r}_{i_\alpha} - \mathbf{r}_{j_\beta}) \rangle$. As expected from a liquid of trimers, g_{22} attains a maximum at the trimer diameter, which is identified from the peak in $|\psi_-|^2$, while g_{12} reaches its maximum at the same position as the probability distribution $|\psi_{12}(\mathbf{r}_1 - \mathbf{r}_2)|^2 = \int d^2 r_3 |\psi(\mathbf{r}_1 - \mathbf{r}_2, \mathbf{r}_1 - \mathbf{r}_3)|^2$.

In Fig. 4a we present the finite size scaling of the low-temperature ρ_- as a function of density. This, together with scaling of the superfluid fraction in the two layers shown in Appendix D, enable us to identify a quantum phase transition (QPT) from the TSF into a state where θ_- orders as well. For the system we have studied numerically the transition occurs at a critical density $n_1 = n_c \approx 0.76/a^2$.

Figure 4a also shows that the cross-layer stiffness ρ_{12}, which is responsible for superfluid drag [24], initially increases with density and then levels off for $n_1 > n_c$. This observation, alongside the results for $g_{\alpha\beta}(\mathbf{r})$ presented in Appendix E, supports the scenario where trimers largely maintain their integrity beyond the QPT. For $n_1 > n_c$, parallel independent superfluidity in both layers is established via hops of single excitons between trimers, accompanied by a global rearrangement of the other particles

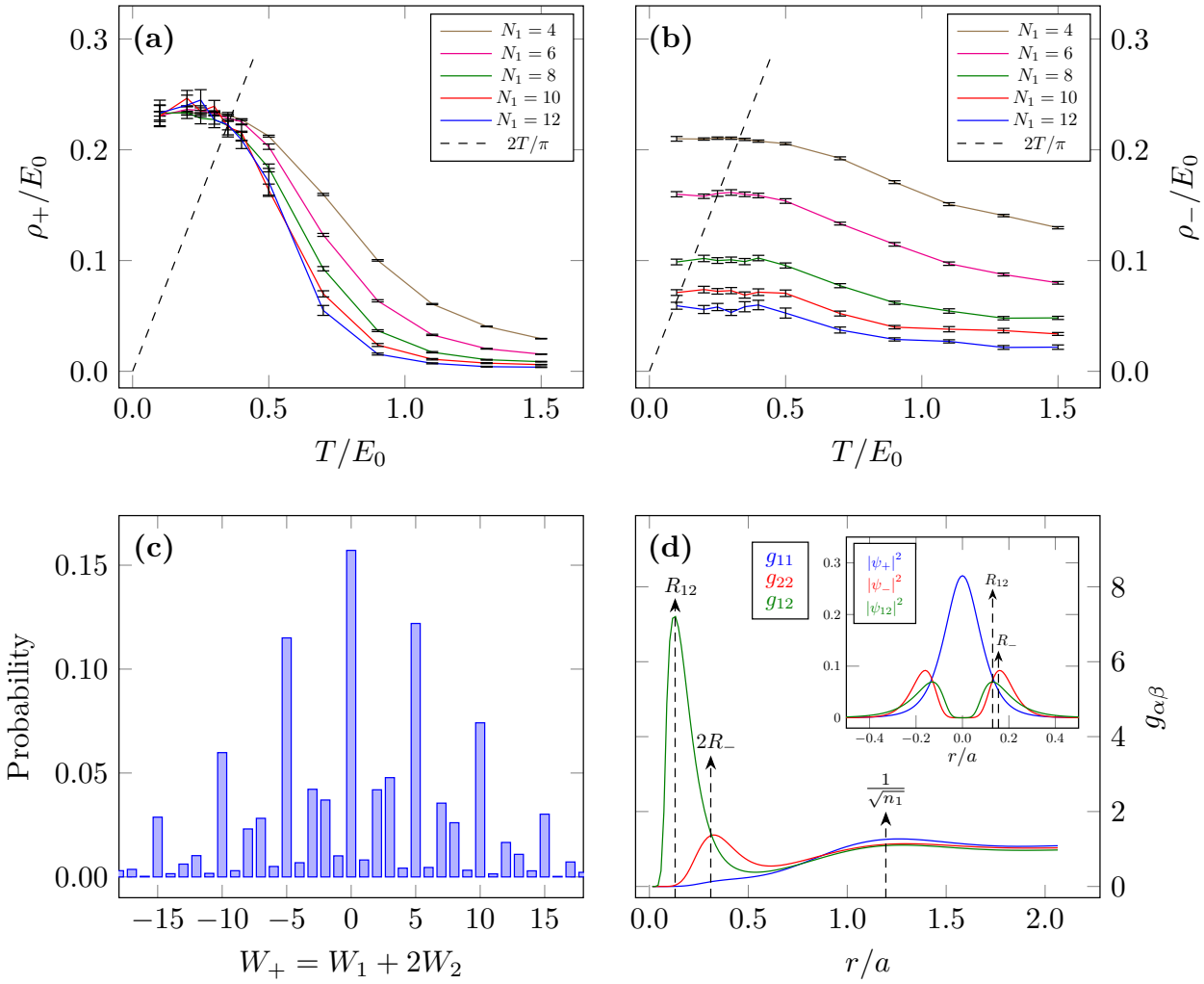


FIG. 3: Evidence for a TSF in a system with $L_z/a = 0.047$ and $n_1 = 0.7/a^2$. (a) and (b) ρ_+ and ρ_- as a function of temperature for various numbers, N_1, of excitons in layer 1. (c) The distribution of the winding number W_+ for the case $N_1 = 12$ and $T = 0.1E_0$. (d) The intralayer (g_{11}, g_{22}) and the interlayer (g_{12}) density-density correlation functions for the same case. They attain a maximum at $1/\sqrt{n_1}$, $2R_-$ and R_{12}, respectively. R_- and R_{12} are the positions of the maxima of $|\psi_-|^2$ and $|\psi_{12}|^2$, as shown in the inset.

into new trimers (see movies [25] and their discussion in Appendix F). The persistence of trimers in the 2SF phase and the resulting large dissipationless drag stand in contrast to the behavior of a bilayer of parallel excitons with equal densities, where dimers dissociate and ρ_{12} rapidly diminishes in the 2SF phase [26]. Furthermore, the exchange symmetry between the layers endows the equal-density transition with a relativistic ($z = 1$) character [14]. In contrast, the system considered here is expected to undergo a more conventional $z = 2$ superfluid transition. The scaling analysis of ρ_-, included in Appendix B, gives evidence to this effect.

V. FINITE TEMPERATURE PHASE DIAGRAM

Having addressed the zero temperature behavior, we now turn to examine the system's thermal phase transitions. The picture for $n_1 < n_c$ is simple, with a BKT disordering transition of θ_+ from the TSF to a normal $U(1) \times U(1)$ symmetric state, as shown by Fig. 3a. To identify possible scenarios for $n_1 > n_c$ let us consider independent condensates in each layer as well as a condensate of trimers. The thermal fluctuations of their phases, $\theta_{1,2}$ and θ_T, are governed by an XY coupling $\sum_\mu \cos(\nabla_\mu \theta)$. Additionally, one needs to account for processes converting a trimer into unbound particles, represented by a term proportional to $\cos(\theta_T - \theta_1 - 2\theta_2)$ [27], which also reduces the symmetry to $U(1) \times U(1)$. At temperatures well below the trimer binding energy and in the vicinity of n_c we replace it by a rigid constraint, leading to the following effective Hamiltonian density in terms of $\theta_{1,2}$ only

$$\mathcal{H} = -\sum_\mu (n_1 - n_c)[\cos(\nabla_\mu \theta_1) + 2\cos(\nabla_\mu \theta_2)] - \sum_\mu \frac{n_c}{3} \cos[\nabla_\mu(\theta_1 + 2\theta_2)]. \quad (3)$$

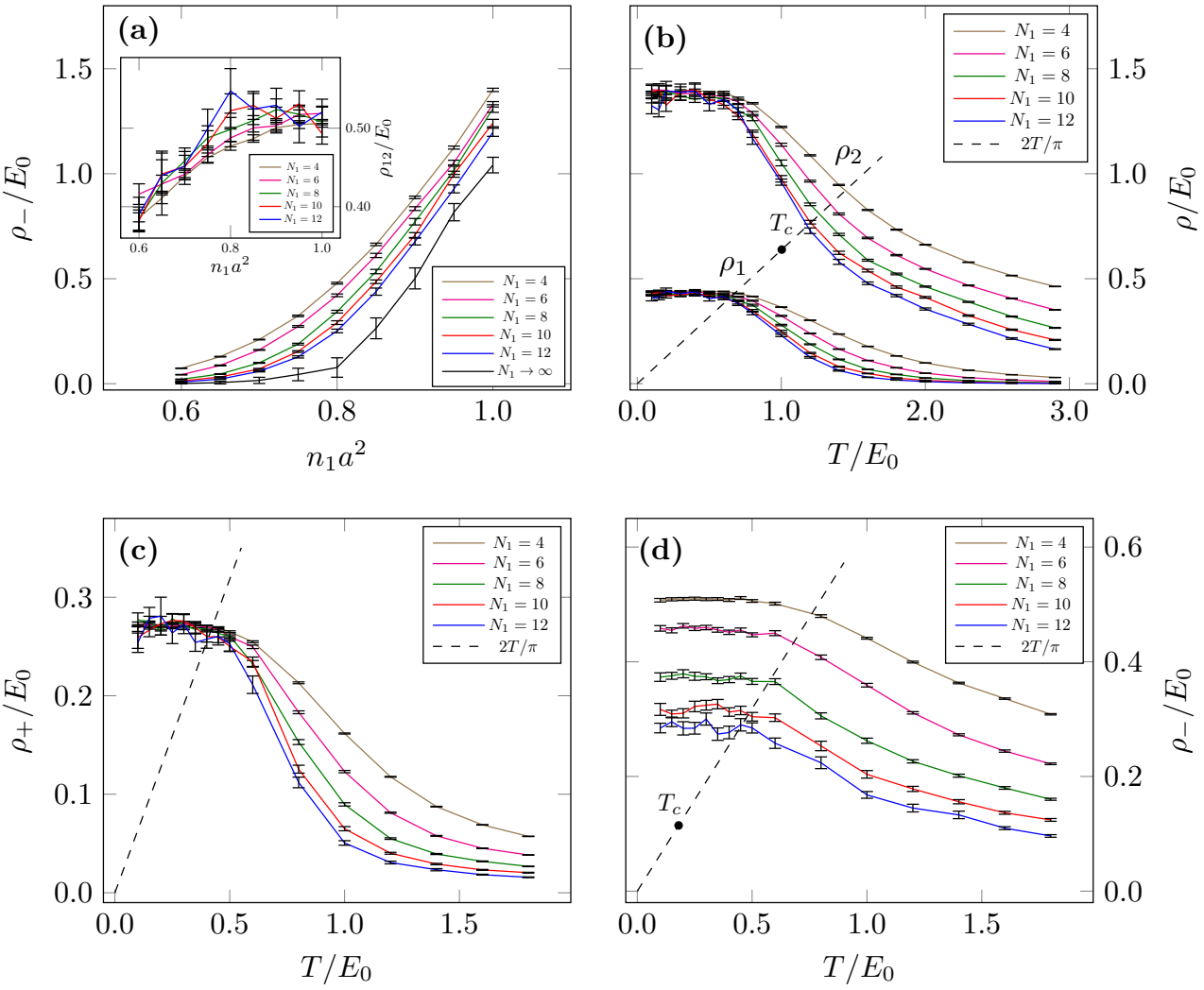


FIG. 4: Finite size scaling of ρ_- as a function of n_1 for a system with $L_z/a = 0.047$ at $T = 0.1E_0$. The inset depicts the cross-stiffness ρ_{12}. (b) $\rho_{1,2}$ as a function of temperature for a system with $n_1 = 0.95/a^2$. (c) and (d) ρ_+ and ρ_- as a function of temperature for a system with $n_1 = 0.81/a^2$. The critical temperatures indicated in (b) and (d) are obtained by finite size scaling of the data for ρ_2 and ρ_-, respectively, as shown in Appendix C.

In the above model, ρ_{12} is proportional to the coefficient of the last term. Based on the observation that at low temperatures ρ_{12} remains approximately constant for $n_1 > n_c$, we have fixed the bare stiffness of the trimers in Eq. (3) to their density to mass ratio at n_c (setting the exciton mass to 1.) Concomitantly, the bare stiffness of the excitonic condensates reflects the excess density in the two layers above n_c.

For n_1 close to n_c, the last term in Eq. (3) is expected to dominate and lead at low temperatures to QLRO in θ_+. Expressing $\theta_{1,2}$ in terms of $\theta_\pm$ and approximating the QLRO by true long-range order in θ_+ we obtain $\mathcal{H} \propto \sum_\mu [\cos(\nabla_\mu 2\theta_-/5) + 2\cos(\nabla_\mu \theta_-/5)]$. The disordering transition of such a Hamiltonian is driven by the proliferation of either 5π or 10π vortices in θ_-, depending on the coupling constants of the two terms [28, 29]. In Appendix H we present Monte Carlo results showing that for small $n_1 - n_c$, model (3) undergoes a BKT transition induced by proliferation of 10π vortices in θ_-. Fig. 4d demonstrates that we find a similar transition from a 2SF to a TSF also in the PIMC data of model (1) with $n_1 = 0.81/a^2$. This is followed at a higher temperature by a transition into the normal state , where the QLRO in θ_+ is lost, as seen in Fig. 4c.

With increasing n_1, the $\cos(\nabla_\mu \theta_2)$ term in Eq. (3) gains importance and eventually becomes dominant, causing θ_2 to develop QLRO. Neglecting the fluctuations in θ_2 one finds $\mathcal{H} \propto \sum_\mu \cos(\nabla_\mu \theta_1)$. Now, the transition out of the low-temperature 2SF phase is best characterized in the 1,2 basis, as it involves loosing superfluidity in layer 1. The higher temperature phase, denoted as SF2, maintains superfluidity in layer 2 while $\rho_1 = \rho_{12} = 0$. It eventually turns into the normal state where $\rho_2 = 0$ as well ($\rho_\alpha \equiv \rho_{\alpha\alpha}$.) Fig. 4b illustrates that this scenario materializes in the excitonic model with $n_1 = 0.95/a^2$. Taken together, the above discussion implies the finite-temperature phase diagram depicted in Fig. 1a.

VI. EXPERIMENTAL CONSIDERATIONS

As a reference, we consider a $MoSe_2$-WSe_2 system [15–20] with $d = 8$ nm and $L_z = 8.6$ nm, see Fig. 1b. We obtain a trimer binding energy $E_B = 0.44$ meV and an average trimer radius of 30 nm. We note that a calculation for a MoS_2-WS_2 bilayer with $d = 8$ nm predicts an interlayer exciton with an approximate binding energy of 75 meV and a radius of 6 nm [30]. The significant size difference between the trimer and its constituent excitons justifies treating the latter as point particles at the relevant length scales. This statement holds true also since our calculation for the same system yields a QPT at $n_c = 2.27 \times 10^9$ cm^{-2}, and $T_c = 0.017$ K for the TSF-Normal transition at $n_1 = 2.1 \times 10^9$ cm^{-2}, corresponding to an inter-trimer distance of about 210 nm.

We find that for fixed L_z/d, E_B changes little with d in the range $5 - 10$ nm, see Appendix A. Within this range, the location of the TSF-2SF QPT is governed by the size of the trimers and not by their binding energy, leading to $n_c \sim 1/L_z^2$. Therefore, we can estimate for a system with $d = 5$ nm and $L_z = 6$ nm that $E_B \simeq 0.3$ meV and $n_c \simeq 4 \times 10^9$ cm^{-2}. For fixed d, both E_B and n_c are increasing functions of d/L_z. Thus, in order to maximize E_B and n_c (and with it T_c of the TSF-Normal transition) it is preferable to make L_z as small as possible.

Interlayer excitons in TMD heterostructures are generated via optical excitation of intralayer excitons, followed by charge transfer between layers due to their inherent (type-II) band alignment [11]. The significant spatial separation between the electron and hole within these interlayer excitons grants them very long lifetimes, on the order of 10 ns [31], much longer than the typical lifetime of intralayer excitons, which is of the order of 10 ps [32]. Consequently, one can isolate the physics associated with the interlayer excitons by introducing a time delay between the optical excitation and the subsequent detection measurement. Furthermore, direct and interlayer excitons are energetically separated by hundreds of meV, making them readily distinguishable in the light emission spectrum [31].

The spatial separation granting interlayer excitons their long lifetimes can also impede their recombination and their subsequent optical detection due to the requirement for charge tunneling. Nonetheless, such excitons have been observed in a TMD heterostructure with a 1 nm hBN spacer [31]. In this case, direct tunneling would be prohibitively slow, suggesting that tunneling instead proceeds via intermediate defect levels within the hBN spacer. Therefore, we propose facilitating tunneling at even larger separations by intentionally doping the hBN spacers with impurities [33]. This approach is supported by a recent demonstration of defect-assisted tunneling through a 4 nm thick carbon-doped hBN barrier [34]. Another option is to form a superlattice of hBN and TMD layers, where the latter act as a stack of effective "defect" states through which tunneling may progress.

Attaining the desired excitonic-density ratio between the bilayers requires selective excitation, which necessitates breaking the symmetry between them. This can be achieved by applying an electric field via top and bottom gates. The field modifies the band alignment in the two bilayers and was shown to tune both the energy and intensity of photoluminescence from interlayer excitons in TMD bilayers, whether in direct contact [15] or separated by an hBN spacer [35]. Another approach, which could also be integrated with an applied field, involves employing distinct TMDs in the two bilayers, such as $MoSe_2$-WSe_2 for one and MoS_2-WS_2 for the other. We note that the symmetry breaking has the additional benefit of enabling differentiation between the light emission originating from the upper and lower excitons.

The excitonic energy shifts, associated with the chemical potentials of the two layers $\mu_{1,2}$, serve as an experimental indicator for a TSF phase. Specifically, in the zero-temperature limit of the TSF phase, $\mu_{1,2}$ should undergo a discontinuous jump when the density of either layer crosses the point $n_2 = 2n_1$. The magnitude of this jump, comparable to the energy difference between trimer and dimer bound states, is expected to vanish in the 2SF phase. While we are unable to calculate $\mu_{1,2}$ at sufficiently low temperatures, we present their high-T dependence on $N_2 - 2N_1$ in Appendix G. In practice, however, the small energy scale of the jump makes its observation challenging, particularly in the presence of unavoidable disorder. Recently, more direct evidence for superfluidity of interlayer excitons was established by measuring the quasi-long-range spatial coherence of their photoluminescence [36], an approach that could similarly be applied in our context. Finally, it is possible to identify the presence of trimers by measuring interlayer drag. This involves driving the upper excitons to drift via a laterally modulated electric field, generated by patterned top gates [37, 38]. A corresponding change in the cloud dynamics of the lower excitons is then sought by monitoring their light emission.

VII. DISCUSSION AND OUTLOOK

We have established the formation of a trimer bound state in a bilayer of antiparallel dipolar excitons. For the case of a 1:2 density ratio between the layers, we have found that although the system is well described as a liquid of bound trimers across the entire studied density range, the resulting low-temperature superfluid still undergoes a quantum phase transition. In the low-density TSF phase, superflow is carried exclusively by trimers. However, across the QPT, new channels involving superflow of individual excitons in the two layers open up in parallel to that of the trimers. The thermal disordering of this 2SF phase is particularly rich, occurring via a cascade of BKT transitions that proceed through a reentrant TSF or a single-layer superfluid phase. Our predictions are directly relevant to experiments probing excitons in TMD heterostructures.

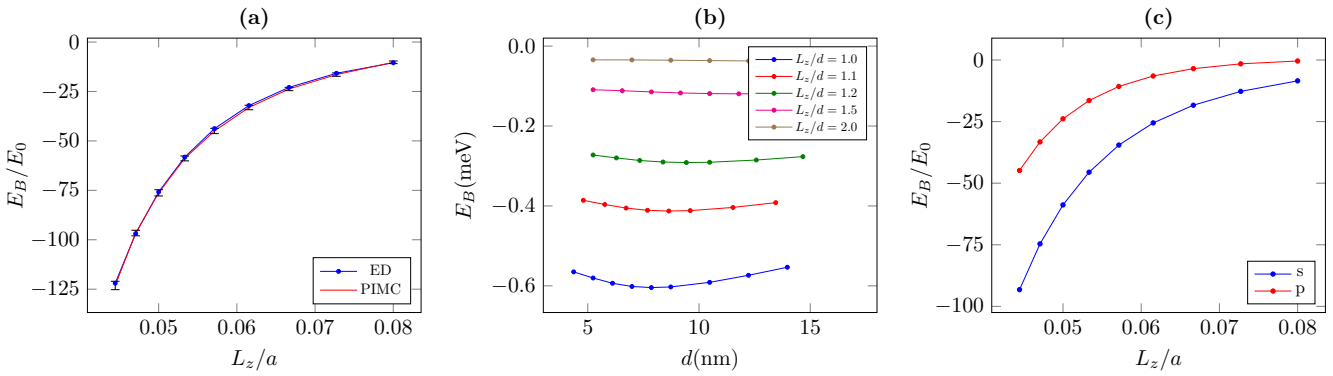


FIG. 5: (a) Comparison between the trimer binding energy as calculated using exact diagonalization and PIMC. (b) The dependence of the trimer binding energy on d, the extent of the exciton along the z-axis, for various values of L_z/d, where L_z is the interlayer separation between dipoles. The data are calculated for a TMD quadrilayer, similar in structure to the one shown in Fig. 1. (c) The binding energy of a dimer with angular momentum $l = 0$ and $l = 1$.

While our primary focus was the 1:2 excitonic density ratio, we now briefly discuss the system's phase diagram as a function of the imbalance away from this point. We do so assuming that at zero temperature and zero imbalance, the system is in the TSF phase. When $N_1 < N_2 < 2N_1$, layer 2 lacks sufficient excitons to bind into trimers with all layer-1 excitons. Consequently, we expect the formation of $2N_1 - N_2$ interlayer dimers coexisting alongside $N_2 - N_1$ trimers, as other configurations, (e.g., involving "reversed" trimers with two layer-1 excitons) exhibit smaller binding energies. At zero temperature both trimers and dimers condense, breaking the full $U(1) \times U(1)$ symmetry. However, for a small imbalance, the dimers are dilute, and thermal disordering of their phases leads to a BKT transition into a TSF phase at a critical temperature that scales linearly with the imbalance. For $N_2 > 2N_1$, the excess layer-2 excitons remain unbound and at low temperature condense in parallel to the trimers. The resulting 2SF phase also undergoes thermal BKT disordering into a TSF phase at a critical temperature that rises linearly with the imbalance.

Looking forward, our work opens several avenues for future research. By increasing the ratio of interaction to kinetic energy, it may be possible to stabilize a crystalline phase of trimers, analogous to phases seen in systems of simple dipoles [39]. Furthermore, extending beyond the bilayer limit, engineering multilayer heterostructures with designed dipole orientations could pave the way for realizing novel composite quasi-particles and exotic correlated states. We leave these outstanding questions to future research.

ACKNOWLEDGMENTS

We thank Ronen Rapaport and Hadar Steinberg for useful discussions. M.Z. acknowledges the support of the Council for Higher Education Scholarships Program for Outstanding Doctoral Students in Quantum Science and Technology. S.G. acknowledges support from the Israel Science Foundation (ISF) Grant no. 586/22 and the US–Israel Binational Science Foundation (BSF) Grant no. 2020264. D.O. acknowledges support from the Israel Science Foundation (ISF) Grant no. 1975/24.

DATA AVAILABILITY

The data that support the findings of this study are available at [25].

Appendix A: Bound State Energies

We have used exact diagonalization, and PIMC simulations in the limit of zero temperature, to obtain the ground state energy of the three-exciton Hamiltonian expressed in terms of $\boldsymbol{\rho}_+ = (\mathbf{r}_2 + \mathbf{r}_3)/2L_z - \mathbf{r}_1/L_z$ and $\boldsymbol{\rho}_- = (\mathbf{r}_2 - \mathbf{r}_3)/2L_z$

$$\mathcal{H} = -\frac{\hbar^2}{2m_X L_z^2}\left(\frac{3}{2}\nabla_+^2 + \frac{1}{2}\nabla_-^2\right) + \frac{D^2}{L_z^3}\left[\frac{1}{8\rho_-^3} - \sum_{\sigma=\pm}\frac{|\boldsymbol{\rho}_+ + \sigma\boldsymbol{\rho}_-|^2 - 2}{\left(|\boldsymbol{\rho}_+ + \sigma\boldsymbol{\rho}_-|^2 + 1\right)^{5/2}}\right], \quad \text{(A1)}$$

where we have omitted the trivial center of mass part. The agreement between the results, as shown in Fig. 5a, attests to the validity of the PIMC calculation.

The binding energy of the trimer bound state depends on the distance d between the layers supporting a dipole, *i.e.* the extent of the exciton along the z-axis, and on the interlayer separation L_z between the dipoles. This is shown in Fig. 5b for a $MoSe_2$-WSe_2 quadrilayer, similar in structure to the one shown in Fig. 1. For fixed L_z/d, the kinetic term in Eq. (A1) scales as $1/d^2$, while the interaction scales as $1/d$. Hence, for sufficiently small d the kinetic energy dominates and leads, due to delocalization effects, to a reduction in the binding energy with decreasing d. In the opposite limit of large d, the interaction part dominates but the strength of the attractive

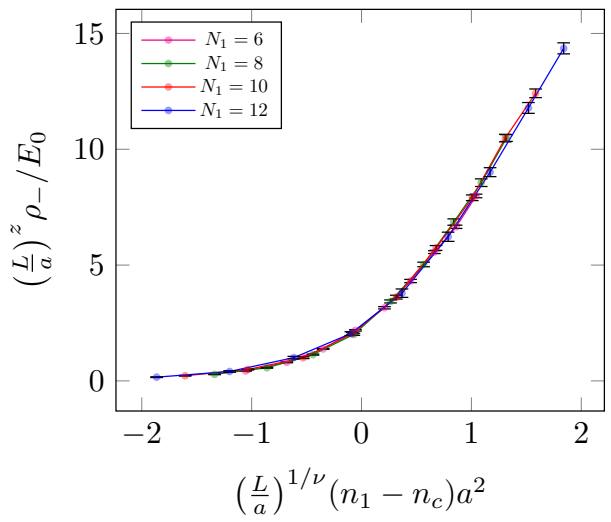


FIG. 6: Data collapse of the ρ_- data using $z = 2$, $\nu = 0.61$ and $n_c = 0.76$.

dipolar potential diminishes with d, and with it the binding energy.

We have also used exact diagonalization to calculate the binding energy of a two-exciton system, described by the Hamiltonian

$$\mathcal{H} = -\frac{\hbar^2}{m_X}\nabla^2 - D^2\frac{r^2 - 2L_z^2}{(r^2 + L_z^2)^{5/2}}. \tag{A2}$$

The results for an s-wave and a p-wave dimer are depicted in Fig. 5c. Evidently, the dimer ground state has zero angular momentum and its binding energy is smaller than that of a trimer state by about 20%, see Fig. 5a.

Appendix B: ρ_- Data Collapse

The zero temperature trimer superfluid phase spontaneously breaks θ_+. The gapless fluctuations in θ_+ are equivalent to particle number fluctuations in the $N_+ = N_1 + 2N_2$ channel, corresponding to adding or removing trimers from the condensate. On the other hand, trimer-breaking excitations that change $N_- = 2N_1 - N_2$ and involve fluctuations in θ_- are gapped in the TSF.

As the density is increased, the gap in the θ_- mode decreases and eventually vanishes at n_c. The nature of the transition depends on whether there is a particle-hole symmetry that makes the gaps involved in increasing and decreasing N_- vanish symmetrically. In such a case the transition is relativistic with a dynamical exponent $z = 1$, and belongs to the 3D XY universality class. In the absence of such a symmetry, as is relevant to our case, the transition is expected to be a non-relativistic, $z = 2$, superfluid transition.

With the above discussion in mind, we can write a scaling form for the stiffness

$$\frac{\rho_-(n_1, L)}{E_0} = \left(\frac{L}{a}\right)^{-z} f\left[\left(\frac{L}{a}\right)^{1/\nu}(n_1 - n_c)a^2\right], \tag{B1}$$

as a function of the rescaled parameter $L^{1/\nu}(n_1 - n_c)$. A curve fit gives our numerical estimates, $\nu = 0.61 \pm 0.04$ and $n_c = 0.758 \pm 0.006$, with $z = 2$, as shown in the curve collapse plot Fig. 6. We note that our estimate of ν is smaller than the 3D XY result $\nu_{\rm 3DXY} = 0.67$, yet larger than the mean field result of $\nu_{\rm MF} = 0.5$. We conjecture that the discrepancy stems from the larger finite-size effects observed in ρ_-, as discussed below.

Appendix C: Finite Size Scaling of Critical Temperatures

The finite size scaling of the critical temperatures of the BKT transitions, deduced from the corresponding stiffnesses, is shown in Fig 7 for three densities across the phase diagram. The data is consistent with $T_c \propto 1/(\log L)^2$ scaling, where L is the system size, as expected from BKT theory.

We find that the critical temperature T_+, calculated from ρ_+ and associated with the TSF-Normal transition, exhibits only weak dependence on L. The same is true for the critical temperature T_1 of the transition between the 2SF and SF2 phases, as calculated from ρ_1. In contrast, the data for ρ_- and ρ_2 show considerably larger finite size effects. For $n_1 = 0.7/a^2$ our finite-size results for T_-, shown in Fig. 7a, are consistent with the vanishing of the low temperature ρ_-, see Fig 4a, and indicate the presence of a zero-temperature TSF. Finite size effects in ρ_- are large at $n_1 = 0.81/a^2$, where the scaling shown in Fig. 7b clearly indicates that $T_+ > T_-$ in the thermodynamic limit, although the reverse is true for all the finite systems that we have simulated. This demonstrates a thermal reentrance of the TSF phase close to the critical density. At higher densities, as depicted in Fig. 7c, T_2 shows more significant changes with L in comparison to T_1, but stays consistently above it thereby establishing the SF2 phase.

Appendix D: Superfluid Fractions

The superfluid fraction $\tilde{n}_\alpha$ in layer α is defined in terms of the one-particle equal-time Green's functions as

$$\tilde{n}_\alpha = \frac{1}{A^2}\int d^2\mathbf{r}\int d^2\mathbf{r}'\left\langle\hat{\psi}_\alpha^\dagger(\mathbf{r})\hat{\psi}_\alpha(\mathbf{r}')\right\rangle, \tag{D1}$$

where A is the system area. In the TSF phase, both θ_1 and θ_2 are disordered and consequently $\tilde{n}_{1,2} = 0$. Conversely, in the ordered 2SF phase both $\tilde{n}_{1,2} \neq 0$. In Fig. 8 we use the expected $1/N_1$ scaling of the superfluid fractions to extrapolate the finite size data to the thermodynamic limit $N_1 \to \infty$. We find that the extrapolated $\tilde{n}_1$ clearly vanishes for $n_1 < 0.79/a^2$ and turns positive at higher densities, consistent with the position of the QPT as deduced from the behavior of ρ_-. The extrapolated $\tilde{n}_2$ follows a similar trend but does not fully vanish in

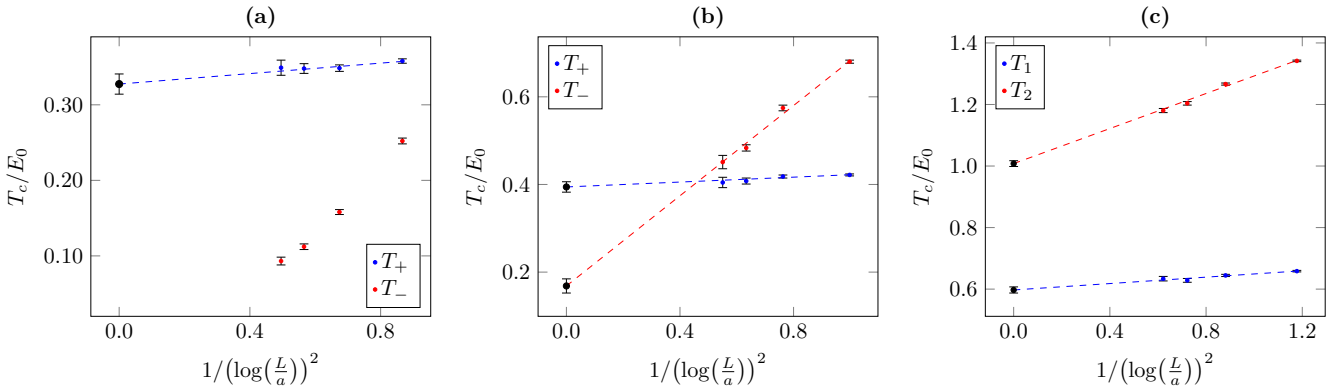


FIG. 7: Finite size scaling of the BKT critical temperatures for (a) $n_1 = 0.7/a^2$. (b) $n_1 = 0.81/a^2$. (c) $n_1 = 0.95/a^2$

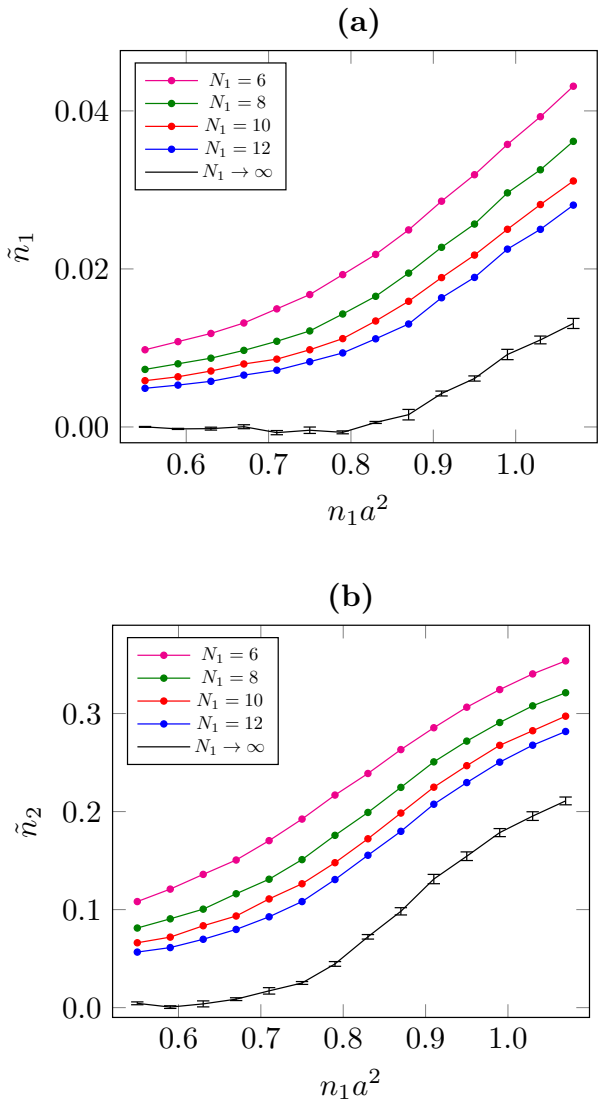


FIG. 8: (a) Finite size scaling of the superfluid fraction in layer 1 as a function density. (b) Finite size scaling of the superfluid fraction in layer 2. The black lines depict the extrapolation to the thermodynamic limit.

the range $0.65 < n_1a^2 < 0.79$. It appears that the layer-2 data is more susceptible to finite size effects, as was already noted in the context of the scaling of the critical temperatures in the previous section.

Appendix E: Density-Density Correlation functions

Fig. 9 depicts the density-density correlation functions $g_{\alpha\beta}$ in the zero-temperature limit, as n_1 is increased across the QPT from the TSF to the 2SF phase. The positions of the peaks in g_{22} and g_{12} are close to $2R_-$ and R_{12} (the positions of the maxima in the single trimer probability distributions $|\psi_-|^2$ and $|\psi_{12}|^2$, respectively), and increase marginally with density. Concomitantly, their height decrease. This shows that the trimers largely maintain their spatial structure across the QPT but that independent motion of excitons is gradually established. The fact that $R_{12} < R_-$, reflects our observation that the top-layer exciton is typically found closer to one of the two bottom-layer excitons and switches between them as the PIMC configuration evolves in imaginary time.

Further insights can be gleaned from the behavior of the first maximum of g_{11} and the second maximum of g_{12} and g_{22}. Their positions $r^*_{\alpha\beta}$, shown in the inset of Fig. 9c, provide a measure for the most probable distance between nearest neighboring trimers. The fact that these peaks continue to exist in the 2SF phase and to follow closely each other is an additional evidence that the trimers do not fall apart when the system exits the TSF phase. The data show that the critical density marks a transition from a $1/\sqrt{n_1}$ scaling of $r^*_{\alpha\beta}$ in the dilute limit where the trimers are largely independent, to $r^*_{\alpha\beta}$ which change little with density in the 2SF phase where trimers can not be pushed closer to each other due to their mutual repulsion.

Finally, as density increases, a bump develops in g_{11} at slightly larger separation than the trimer diameter $2R_-$. This indicates that trimers spend increasingly more time in the vicinity of each other. Such events allow for more effective exchange of excitons between trimers and establish windings by independent excitons around the sample that lead to the 2SF phase.

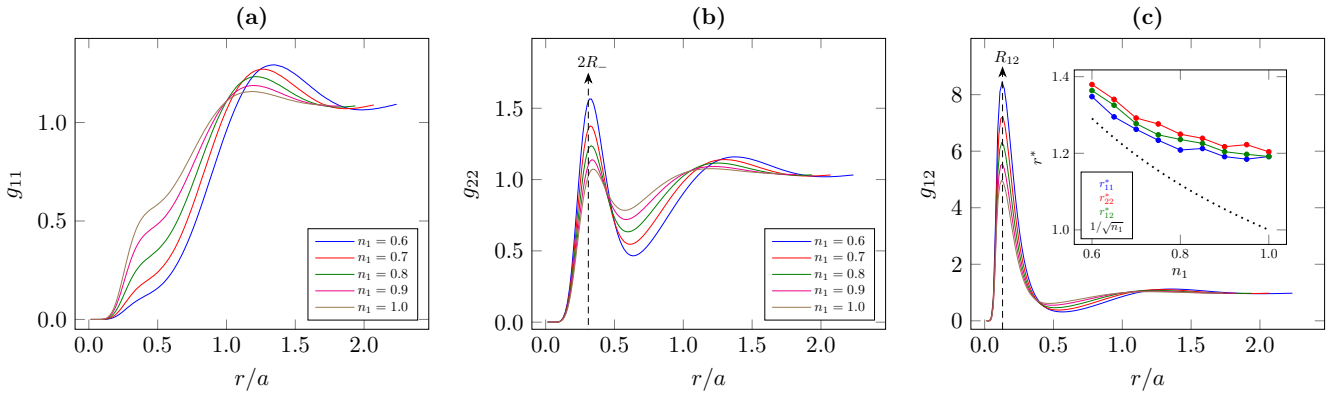


FIG. 9: The density-density correlation functions in the zero-temperature limit for various densities n_1. (a) The peak in g_{11} resides at $1/\sqrt{n_1}$, while the shoulder appears at a separation slightly larger than the trimer diameter $2R_-$, which is also where g_{22} exhibits a peak, as shown in (b). (c) The interlayer correlations peaks at R_{12}, where the probability distribution $|\psi(\mathbf{r_1} - \mathbf{r_2})|^2$ attains its maximum. The inset depicts the positions $r^*_{\alpha\beta}$ of the first maximum in g_{11} and the second maximum of g_{12} and g_{22} as a function of n_1.

Appendix F: Exciton Winding

To gain insights into the nature of exciton winding we include two movies in [40] showing the imaginary time evolution of the exciton configuration over $\tau \in [0, \beta]$ at a temperature $T = 0.1E_0$. Red and blue colors denote layer-1 and layer-2 particles, respectively. At each time slice we group the particles into trios by minimizing the sum over all trios of the distance between the layer-1 particle and its layer-2 partners within the trio. To help follow the evolution of the windings we display next to each particle its instantaneous winding number, which increases or decreases by one when it crosses the dashed boundary from left to right or from right to left, respectively. The title depicts the imaginary time, the sum total of the windings $W_{1,2}$ of particles in each layer, and the relative winding $W_- = 2W_1 - W_2$. The variance of $W_-(\tau = \beta)$ determines ρ_-.

The movie TSF.mp4 [40] follows an $n_1 a^2 = 0.7$ system that is in a TSF phase. Clearly, the particles are bound into trimers, and crossings of the boundary typically involve an entire trimer. During such events W_- becomes momentarily nonzero, but then vanishes again when the trimer completes its crossing. Alternatively, two trimers may come together from both sides of the boundary and exchange a pair of particles between them. These events also maintain a zero W_-, which is the hallmark of a TSF.

The movie 2SF.mp4 [40] follows an $n_1 a^2 = 0.95$ system that is in a 2SF phase. One observes that the particles still spend most of the time within well-defined trimers that follow the dynamics described above. However, there is an increased number of cases where a layer-2 particle lingers away from its partners. Instances of this type allow for a new type of winding events where such a particle crosses the boundary and joins a new trimer, without its old partners crossing the boundary as well. This is followed by a global rearrangement of the particles into a new configuration of trimers. The net result is a change in W_- that can establish non-vanishing ρ_- and hence a 2SF phase.

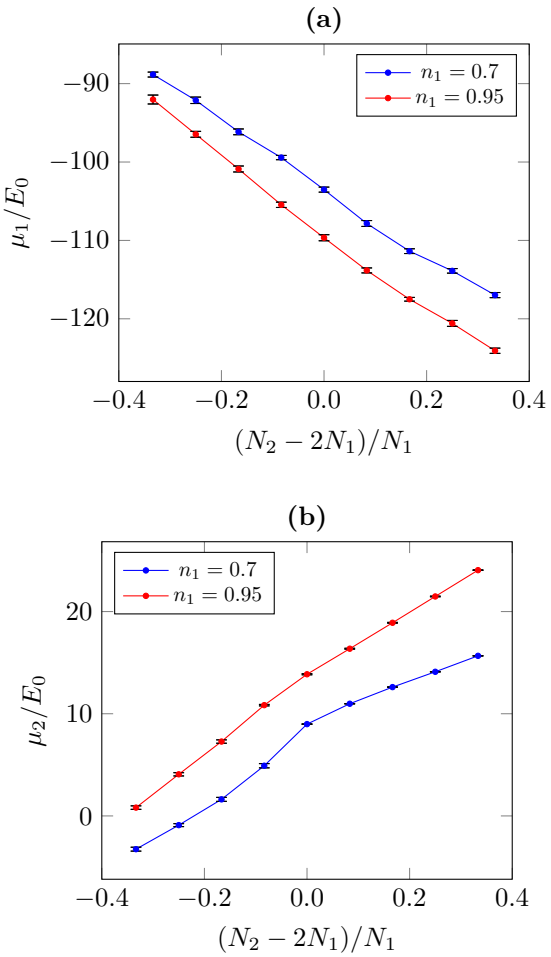


FIG. 10: The chemical potentials of the two layers as a function of the relative deviation from the point $N_2 = 2N_1$. The data are shown for a system with $N_1 = 12$ at the two indicated densities. (a) μ_1 at $T = 2.5E_0$, (b) μ_2 at $T = 1.5E_0$.

Appendix G: Chemical Potentials

We calculate the finite temperature chemical potentials of both layers $\mu_\alpha = F(N_\alpha+1,T)-F(N_\alpha,T)$ as a function of the relative deviation $(N_2-2N_1)/N_1$ from the 1 : 2 density ratio. We control the deviation by fixing N_1 and varying N_2. We consider two densities $n_1 = 0.7$ and $n_1 = 0.95$, where the low-temperature phase of the system is a TSF and 2SF, respectively. However, we were unable to obtain reliable $\mu_{1,2}$ data within the superfluid phases. Therefore, Fig. 10 depicts results for μ_1 at $T = 2.5E_0$ and for μ_2 at $T = 1.5E_0$, where the system is in its normal state.

As noted in the Discussion, when $N_1 < N_2 < 2N_1$, $2N_1 - N_2$ interlayer dimers, each comprising a pair of excitons from the two layers, are expected to form alongside the trimers. Under such conditions, the addition of an exciton to layer 1 converts a trimer into a pair of dimers. In the dilute limit this leads to a reduction of the energy by $2E_D - E_T \simeq 60E_0$, where E_D and E_T are the dimer and trimer binding energies, respectively. The gain in free energy is further enhanced by the attractive interaction between the added exciton and the dipoles in layer 2. Its effect outweighs that of the repulsion within layer 1 due to the higher density in layer 2. Consequently, μ_1 is expected to be large and negative, increasing in magnitude as N_2 increases. The data presented in Fig. 10a align with this expectation.

Conversely, the addition of an exciton to layer 2 of a system with $N_1 < N_2 < 2N_1$ converts a dimer into a trimer and reduces the energy by $E_T - E_D \simeq 20E_0$. However, the interaction of the added exciton with the other dipoles modifies this result. The dominant role is played by the repulsion from the other layer-2 excitons, which diminishes the energetic gain and leads to a negative μ_2 whose magnitude is smaller than $E_T - E_D$ and decreases with N_2, as shown in Fig. 10b.

Excess excitons in layer 2 remain unbound for $N_2 > 2N_1$. Adding a layer-1 exciton binds two layer-2 excitons into a trimer, which in the dilute limit reduces the energy by $E_T \simeq 100E_0$. The attraction from layer-2 excitons further reduces the energy, thus making μ_1 more negative with increasing N_2, see Fig. 10a. Since additional layer-2 dipoles do not bind when $N_2 > N_1$ and are primarily affected by intralayer repulsion, μ_2 is positive and increases with N_2 in this parameter range, as demonstrated by Fig. 10b.

We expect that a TSF leads to a discontinuous jump in μ_1 and μ_2 at $T = 0$ and $N_2 = 2N_1$, which in the dilute limit approach $-2(E_T - E_D)$ and $E_T - E_D$, respectively. The jump gets smoother as temperature is increased. Although we are unable to reach the required low temperatures, we note that μ_2 exhibits a kink at $N_2 = 2N_1$ for $n_1 = 0.7$.

Appendix H: Effective XY Model

We employ classical Monte Carlo worm-algorithm simulations to study the effective XY model

$$\begin{aligned}\mathcal{H} &= -\sum_\mu \left\{(n_1-n_c)\left[\cos(\nabla_\mu\theta_1)+2\cos(\nabla_\mu\theta_2)\right]+\frac{n_c}{3}\cos\left[\nabla_\mu(\theta_1+2\theta_2)\right]\right\}\\ &= -\sum_\mu \left\{(n_1-n_c)\left[\cos\left(\nabla_\mu\frac{\theta_+ +2\theta_-}{5}\right)+2\cos\left(\nabla_\mu\frac{2\theta_+-\theta_-}{5}\right)\right]+\frac{n_c}{3}\cos\left(\nabla_\mu\theta_+\right)\right\}\end{aligned} \tag{H1}$$

on an $L\times L$ lattice. To this end, we use the loop representation of the partition function as a sum over configurations of closed current loops in both layers

$$\mathcal{Z} = \sum_{\left\{\sum_\mu \nabla_\mu j_\mu^\alpha = 0\right\}} \prod_{\mu,\mathbf{r}}\left[\sum_{m=-\infty}^{\infty} I_m\left(\frac{n_c}{3T}\right) I_{(j_\mu^1-m)}\left(\frac{n_1-n_c}{T}\right) I_{(j_\mu^2-2m)}\left(2\frac{n_1-n_c}{T}\right)\right]. \tag{H2}$$

Here, T is the temperature, I_m are the modified Bessel functions of the first kind, and $j_\mu^\alpha(\boldsymbol{r})$ is the integer current variable associated with the bond emanating from site $\boldsymbol{r}$ on layer α along the μ direction. Within this representation the stiffnesses are calculated as

$$\rho_{\alpha\beta} = T\left\langle\left(\sum_{\mu,\mathbf{r}} j_\mu^\alpha\right)\left(\sum_{\mu,\mathbf{r}} j_\mu^\beta\right)\right\rangle. \tag{H3}$$

We set $n_c = 1$ and consider two regimes, one near the critical density at $n_1 = 1.05$, and the other further away from the critical density at $n_1 = 2$.

1. The 2SF-TSF-Normal Transitions

At $n_1 = 1.05$, the bare stiffness associated with the first two terms in Eq. (H1) is small and the trimer term

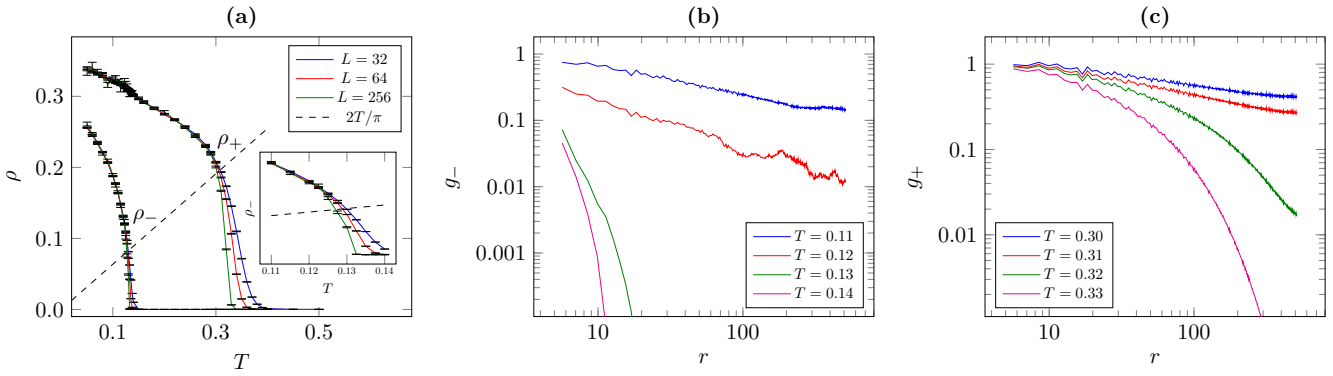


FIG. 11: (a) The temperature dependence of the stiffnesses, ρ_- and ρ_+, associated with the phases $\theta_-/5$ and θ_+, for $n_1 = 1.05$. Both develop a jump when crossing the $2T/\pi$ line, as the system size increases. The inset zooms on the vicinity of the jump in ρ_-. (b) and (c) The θ_- and θ_+ two-point correlations as a function of separation for a system with $L = 1024$ at various temperatures.

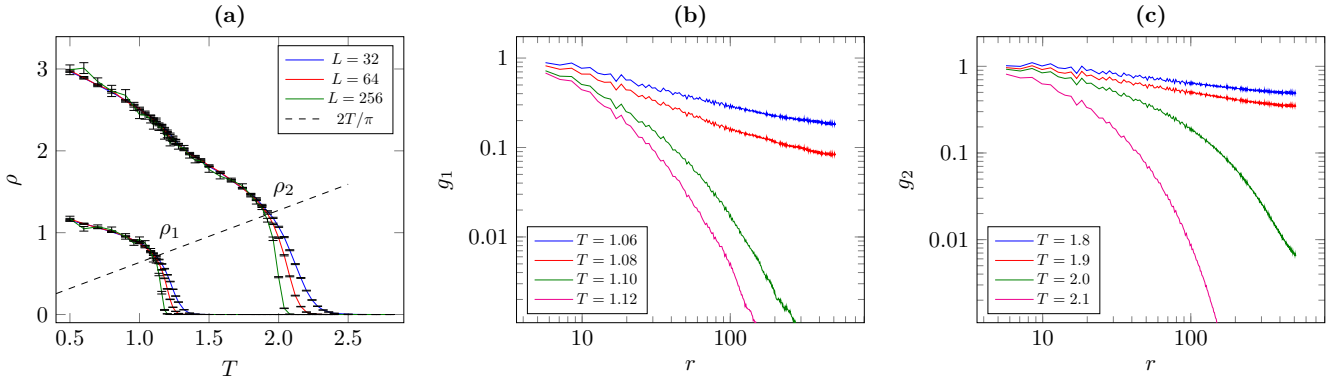


FIG. 12: (a) The temperature dependence of the stiffnesses, ρ_1 and ρ_2, associated with the phases θ_1 and θ_2, for $n_1 = 2$. Both develop a jump when crossing the $2T/\pi$ line, as the system size increases. (b) and (c) The θ_1 and θ_2 two-point correlations as a function of separation for a system with $L = 1024$ at various temperatures.

$\sum_\mu \cos(\nabla_\mu \theta_+)$ dominates. Consequently, the transition out of the low temperature 2SF phase is driven by the proliferation of θ_- vortices. These are constrained to obey $m_1 + 2m_2 = 0$, where m_α is the vorticity in layer α, since θ_+ retains its QLRO through the transition to the TSF phase.

There are two possible scenarios for the disordering of θ_- [28, 29]. The first involves θ_- vortices with a 10π phase twist ($m_1 = 2$, $m_2 = -1$) caused by the $\theta_-/5$ term in Eq. (H1). Their proliferation induces a BKT transition with a jump of $2T_c/\pi$ in the stiffness $\rho_- = 4\rho_1 + \rho_2 - 4\rho_{12}$ associated with the phase $\theta_-/5$. Alternatively, the model may undergo an Ising-like transition into a nematic phase, followed by a BKT transition due to proliferation of θ_- vortices with a 5π phase twist ($m_1 = 1$, $m_2 = -1/2$). Such a transition would be accompanied by an $8T_c/\pi$ jump in ρ_-. Fig. 11a gives evidence in favor of the first scenario by showing that as L increases, ρ_- develops a jump when crossing the $2T/\pi$ line. Concomitantly, as shown by Fig. 11b, the decay of the θ_- correlation function $g_-(r) = \left\langle e^{i[\theta_-(r) - \theta_-(0)]} \right\rangle$ changes from power-law to exponential when the temperature is raised through the location of the ρ_- jump in Fig. 11a. As the temperature is further increased, QLRO in θ_+ is lost due to proliferation of 2π vortices in θ_+, see Fig. 11a and Fig. 11c.

2. The 2SF-SF2-Normal Transitions

At $n_1 = 2$, the dominant term in Eq. (H1) is $\sum_\mu \cos(\nabla_\mu \theta_2)$. Thus, θ_2 retains QLRO across the low-temperature 2SF-SF2 BKT transition, while θ_1 becomes disordered by proliferation of 2π vortices. The transition is identified by the onset of a jump in ρ_1 as it crosses the $2T/\pi$ line and by the accompanying exponential decay of the two-point θ_1 correlations $g_1(r) = \left\langle e^{i[\theta_1(r) - \theta_1(0)]} \right\rangle$, see Fig. 12a and Fig. 12b. The phase θ_2 undergoes a similar disordering transition at a higher temperature due to proliferation of 2π vortices, as shown by Fig. 12a and Fig. 12c. The system then exits the SF2 phase into the normal state.

[1] T. Lahaye, C. Menotti, L. Santos, M. Lewenstein, and T. Pfau, The physics of dipolar bosonic quantum gases, Rep. Prog. Phys. **72**, 126401 (2009).

[2] L. Chomaz, I. Ferrier-Barbut, F. Ferlaino, B. Laburthe-Tolra, B. L. Lev, and T. Pfau, Dipolar physics: a review of experiments with magnetic quantum gases, Rep. Prog. Phys. **86**, 026401 (2022).

[3] A. Griesmaier, J. Werner, S. Hensler, J. Stuhler, and T. Pfau, Bose-Einstein condensation of chromium, Phys. Rev. Lett. **94**, 160401 (2005).

[4] M. Lu, N. Q. Burdick, S. H. Youn, and B. L. Lev, Strongly dipolar Bose-Einstein condensate of dysprosium, Phys. Rev. Lett. **107**, 190401 (2011).

[5] K. Aikawa, A. Frisch, M. Mark, S. Baier, A. Rietzler, R. Grimm, and F. Ferlaino, Bose-Einstein condensation of erbium, Phys. Rev. Lett. **108**, 210401 (2012).

[6] L. Chomaz, D. Petter, P. Ilzhöfer, G. Natale, A. Trautmann, C. Politi, G. Durastante, R. M. W. van Bijnen, A. Patscheider, M. Sohmen, M. J. Mark, and F. Ferlaino, Long-lived and transient supersolid behaviors in dipolar quantum gases, Phys. Rev. X **9**, 021012 (2019).

[7] L. Tanzi, E. Lucioni, F. Famà, J. Catani, A. Fioretti, C. Gabbanini, R. N. Bisset, L. Santos, and G. Modugno, Observation of a dipolar quantum gas with metastable supersolid properties, Phys. Rev. Lett. **122**, 130405 (2019).

[8] F. Böttcher, J.-N. Schmidt, M. Wenzel, J. Hertkorn, M. Guo, T. Langen, and T. Pfau, Transient supersolid properties in an array of dipolar quantum droplets, Phys. Rev. X **9**, 011051 (2019).

[9] L. V. Butov, Condensation and pattern formation in cold exciton gases in coupled quantum wells, J. Phys. Condens. Matter **16**, R1577 (2004).

[10] R. Rapaport and G. Chen, Experimental methods and analysis of cold and dense dipolar exciton fluids, J. Phys. Condens. Matter **19**, 295207 (2007).

[11] E. Paik, L. Zhang, K. F. Mak, J. Shan, and H. Deng, Excitons and polaritons in two-dimensional transition metal dichalcogenides: a tutorial, Adv. Opt. Photon. **16**, 1064 (2024).

[12] C. Hubert, Y. Baruchi, Y. Mazuz-Harpaz, K. Cohen, K. Biermann, M. Lemeshko, K. West, L. Pfeiffer, R. Rapaport, and P. Santos, Attractive dipolar coupling between stacked exciton fluids, Phys. Rev. X **9**, 021026 (2019).

[13] D. J. Choksy, C. Xu, M. M. Fogler, L. V. Butov, J. Norman, and A. C. Gossard, Attractive and repulsive dipolar interaction in bilayers of indirect excitons, Phys. Rev. B **103**, 045126 (2021).

[14] M. Zimmerman, R. Rapaport, and S. Gazit, Collective interlayer pairing and pair superfluidity in vertically stacked layers of dipolar excitons, Proc. Natl. Acad. Sci. U.S.A. **119**, e2205845119 (2022).

[15] P. Rivera, J. R. Schaibley, A. M. Jones, H. R. Gutiérrez, J. Yan, D. Mandrus, F. Wang, W. Yao, X. Xu, M. J. Kim, J. Park, D. Liebig, Y. Xu, N. C. Plumb, D. P. Simmers, and R. M. Wallace, Observation of long-lived interlayer excitons in monolayer $MoSe_2$–WSe_2 heterostructures, Nat. Commun. **6**, 6242 (2015).

[16] P. Rivera, K. L. Seyler, H. Yu, J. R. Schaibley, J. Yan, D. G. Mandrus, W. Yao, and X. Xu, Valley-polarized exciton dynamics in a 2D semiconductor heterostructure, Science **351**, 688 (2016).

[17] L. A. Jauregui, A. Y. Joe, K. Pistunova, D. S. Wild, A. A. High, Y. Zhou, G. Scuri, K. D. Greve, A. Sushko, C.-H. Yu, T. Taniguchi, K. Watanabe, D. J. Needleman, M. D. Lukin, H. Park, and P. Kim, Electrical control of interlayer exciton dynamics in atomically thin heterostructures, Science **366**, 870 (2019).

[18] L. Zhang, R. Gogna, G. W. Burg, J. Horng, E. Paik, Y.-H. Chou, K. Kim, E. Tutuc, and H. Deng, Highly valley-polarized singlet and triplet interlayer excitons in van der Waals heterostructure, Phys. Rev. B **100**, 041402 (2019).

[19] E. Liu, E. Barre, J. van Baren, D. S. Komatsu, D. K. Singh, S. A. Lee, Y. J. Yuan, K. Watanabe, T. Taniguchi, P. Jarillo-Herrero, D. Lu, and D. A. Reis, Signatures of moiré trions in $WSe_2/MoSe_2$ heterobilayers, Nature **594**, 46–50 (2021).

[20] M. Brotons-Gisbert, H. Baek, A. Campbell, K. Watanabe, T. Taniguchi, and B. D. Gerardot, Moiré-trapped interlayer trions in a charge-tunable $WSe_2/MoSe_2$ heterobilayer, Phys. Rev. X **11**, 031033 (2021).

[21] D. M. Ceperley, Path integrals in the theory of condensed helium, Rev. Mod. Phys. **67**, 279 (1995).

[22] M. Boninsegni, N. Prokof'ev, and B. Svistunov, Worm algorithm for continuous-space path integral Monte Carlo simulations, Phys. Rev. Lett. **96**, 070601 (2006).

[23] E. L. Pollock and D. M. Ceperley, Path-integral computation of superfluid densities, Phys. Rev. B **36**, 8343 (1987).

[24] K. Sellin and E. Babaev, Superfluid drag in the two-component Bose-Hubbard model, Phys. Rev. B **97**, 094517 (2018).

[25] P. P. Belgaonkar, M. Zimmerman, S. Gazit, and D. Orgad, Trimer superfluidity of antiparallel dipolar excitons in a bilayer heterostructure, 10.5281/zenodo.16165694 (2025).

[26] A. Macia, G. E. Astrakharchik, F. Mazzanti, S. Giorgini, and J. Boronat, Single-particle versus pair superfluidity in a bilayer system of dipolar bosons, Phys. Rev. A **90**, 043623 (2014).

[27] A. Kuklov, N. Prokof'ev, and B. Svistunov, Superfluid-superfluid phase transitions in a two-component Bose-Einstein condensate, Phys. Rev. Lett. **92**, 030403 (2004).

[28] D. H. Lee and G. Grinstein, Strings in two-dimensional classical XY models, Phys. Rev. Lett. **55**, 541 (1985).

[29] D. B. Carpenter and J. T. Chalker, The phase diagram of a generalised XY model, J. Phys. Condens. Matter **1**, 4907 (1989).

[30] M. Van der Donck and F. M. Peeters, Interlayer excitons in transition metal dichalcogenide heterostructures, Phys. Rev. B **98**, 115104 (2018).

[31] E. V. Calman, M. M. Fogler, L. V. Butov, S. Hu, A. Mishchenko, and A. K. Geim, Indirect excitons in van der Waals heterostructures at room temperature, Nat. Commun. **9**, 1895 (2018).

[32] G. Wang, A. Chernikov, M. M. Glazov, T. F. Heinz, X. Marie, T. Amand, and B. Urbaszek, Colloquium: Excitons in atomically thin transition metal dichalcogenides, Rev. Mod. Phys. **90**, 021001 (2018).

[33] L. Weston, D. Wickramaratne, M. Mackoit, A. Alkauskas, and C. G. Van de Walle, Native point defects and impurities in hexagonal boron nitride, Phys. Rev. B **97**, 214104 (2018).

[34] Y. Seo, Y. Tsuji, M. Onodera, R. Moriya, Y. Zhang, K. Watanabe, T. Taniguchi, and T. Machida, Spectrum of tunneling transport through phonon-coupled defect states in a carbon-doped hexagonal boron nitride barrier, Nano Lett. **24**, 13733 (2024).

[35] J. Kistner-Morris, A. Shi, E. Liu, T. Arp, F. Farahmand, T. Taniguchi, K. Watanabe, V. Aji, C. H. Lui, and N. Gabor, Electric-field tunable Type-I to Type-II band alignment transition in $MoSe_2/WS_2$ heterobilayers, Nat. Commun. **15**, 4075 (2024).

[36] J. Cutshall, F. Mahdikhany, A. Roche, D. N. Shanks, M. R. Koehler, D. G. Mandrus, T. Taniguchi, K. Watanabe, Q. Zhu, B. J. LeRoy, and J. R. Schaibley, Imaging interlayer exciton superfluidity in a 2D semiconductor heterostructure, Sci. Adv. **11**, eadr1772 (2025).

[37] D. Unuchek, A. Ciarrocchi, A. Avsar, K. Watanabe, T. Taniguchi, and A. Kis, Room-temperature electrical control of exciton flux in a van der Waals heterostructure, Nature **560**, 340 (2018).

[38] D. N. Shanks, F. Mahdikhanysarvejahany, C. Muccianti, A. Alfrey, M. R. Koehler, D. G. Mandrus, T. Taniguchi, K. Watanabe, H. Yu, B. J. LeRoy, and J. R. Schaibley, Nanoscale trapping of interlayer excitons in a a 2D semiconductor heterostructure, Nano Lett. **21**, 5641 (2021).

[39] H. P. Büchler, E. Demler, M. Lukin, A. Micheli, N. Prokof'ev, G. Pupillo, and P. Zoller, Strongly correlated 2D quantum phases with cold polar molecules: Controlling the shape of the interaction potential, Phys. Rev. Lett. **98**, 060404 (2007).

[40] The Supplemental Material at `https://doi.org/10.1103/zn5r-2vrb` includes two movies demonstrating particle windings in the TSF and 2SF phases.